PFC/JA-90-4

LARGE-AMPLITUDE COHERENT STRUCTURES IN NONNEUTRAL PLASMAS WITH CIRCULATING ELECTRON FLOW[†]

by

Ronald C. Davidson
Hei-Wai Chan
Chiping Chen
Steven Lund

February, 1990

Presented at the Topical Conference on Research Trends in Nonlinear and Relativistic Effects in Plasmas (La Jolla, February, 1990).

[†]Research supported in part by the Office of Naval Research, the Department of Energy High Energy Physics Division, and the Naval Research Laboratory Plasma Physics Division.

LARGE-AMPLITUDE COHERENT STRUCTURES IN NONNEUTRAL PLASMAS WITH CIRCULATING ELECTRON FLOW[†]

Ronald C. Davidson, Hei-Wai Chan, Chiping Chen and Steven Lund
Plasma Fusion Center
Massachusetts Institute of Technology
Cambridge, Massachusetts 02139

ABSTRACT

The nonlinear dynamics of nonneutral plasmas with circulating electron flow is often characterized by large-amplitude coherent structures. Use is made of a cold-fluid guiding-center model to investigate the properties of stationary, two-dimensional, large-amplitude vortex structures in a low-density ($s_e = \omega_{pe}^2/\omega_{ce}^2 \ll 1$) nonneutral plasma column confined by an axial magnetic field $B_0\hat{e}_z$. In addition, particle-in-cell computer simulation studies are presented which describe the nonlinear evolution of a high-density ($s_e = \omega_{pe}^2/\omega_{ce}^2 \sim 1$) nonneutral electron layer in a relativistic cylindrical magnetron, including the formation of a large-amplitude "spoke" structure in the circulating electron density.

I. INTRODUCTION

The formation and evolution of large-amplitude coherent structures play an important role in describing the nonlinear dynamics of nonneutral plasmas[1] with circulating electron flow. This is true in systems ranging from low-density ($s_e = \omega_{pe}^2/\omega_{ce}^2 \ll 1$) rotating nonneutral plasmas initially subject to the diocotron instability, to high-density ($s_e = \omega_{pe}^2/\omega_{ce}^2 \sim 1$) circulating nonneutral electron layers in conventional and relativistic magnetrons. Here, ω_{pe} is the electron plasma frequency, ω_{ce} is the electron cyclotron frequency associated with the confining magnetic field, and $s_e = \omega_{pe}^2/\omega_{ce}^2$ is a measure of the self-field intensity.

This paper makes use of a cold-fluid guiding-center model to investigate the properties of stationary, two-dimensional,

---

[†]Research supported in part by the Office of Naval Research, the Department of Energy High Energy Physics Division, and the Naval Research Laboratory Plasma Physics Division.

large-amplitude vortex structures in a low-density nonneutral plasma column (Sec. II). In addition, particle-in-cell computer simulations are presented which describe the nonlinear evolution of a high-density nonneutral electron layer in a relativistic cylindrical magnetron, including the formation of a large-amplitude "spoke" structure in the circulating electron density (Sec. III).

By way of background, one of the most ubiquitous properties of low-density nonneutral plasma initially subject to the diocotron instability[2-12] is the development of long-lived, rotating vortex structures[13] during the nonlinear evolution of the system. This has been observed experimentally in annular electron layers,[14,15] intense propagating annular electron beams,[16] nonneutral plasma columns with[17,18] and without[19-21] central conductors, and in computer simulation studies.[18] The fact that long-lived coherent structures exist in these systems for many rotation periods and thousands of cyclotron periods suggests the existence of large-amplitude solutions which are stationary in the rotating frame. In Sec. II, use is made of a cold-fluid guiding-center model to investigate the properties of large-amplitude stationary vortex structures in a low-density nonneutral plasma column with $s_e = \omega_{pe}^2/\omega_{ce}^2 \ll 1$.

In contrast, magnetrons operate with dense nonneutral electron layers characterized by $s_e = \omega_{pe}^2/\omega_{ce}^2 \sim 1$. In relativistic magnetrons,[22-30] pulsed high-voltage diodes are used to generate microwaves at gigawatt power levels. Although magnetrons are widely used as microwave sources, a fundamental understanding of the underlying interaction physics is still being developed,[31] particularly in the nonlinear regime. Part of the theoretical challenge is associated with the fact that the electrons emitted from the cathode interact with the electromagnetic waves excited in the anode-cathode gap in a highly nonlinear way. This is manifest through a strong azimuthal bunching of the electrons and the formation of a large-amplitude spoke structure in the circulating electron density. In this regard, computer simulation studies[32-35] provide a particularly valuable approach to analyze the interaction physics and nonlinear electrodynamics in magnetrons. In Sec. II, we summarize recent

computer simulations[35] of the multiresonator, cylindrical A6 magnetron configuration[26] using the two-dimensional particle-in-cell code MAGIC,[36] including the formation of a coherent, large-amplitude spoke structure in the circulating electron density.

II. LARGE-AMPLITUDE VORTEX STRUCTURES IN LOW-DENSITY NONNEUTRAL PLASMA

In this section, use is made of a cold-fluid guiding-center model (Sec. II.A) to investigate the properties of stationary coherent structures in a low-density ($s_e = \omega_{pe}^2/\omega_{ce}^2 \ll 1$) nonneutral plasma column (Sec. II.B). Particular examples of large-amplitude $\ell = 1$ and $\ell = 2$ vortex structures are then presented (Sec. II.C).

A. Nonrelativistic Guiding-Center Model

We consider a low-density nonneutral electron plasma in cylindrical geometry with

$$\frac{\omega_{pe}^2}{\omega_{ce}^2} = \frac{4\pi\, n_e(\underset{\sim}{x},t) m_e c^2}{B_0^2} \ll 1 \ . \tag{1}$$

Here, m_e is the electron mass, c is the speed of light in vacuo, and $n_e(\underset{\sim}{x},t)$ is the electron density. The electrons are confined radially by a uniform axial magnetic field $B_0\hat{\underset{\sim}{e}}_z$, and cylindrical conducting walls are located at $r = a$ and $r = b$ (Fig. 1). The case in which the central conductor is absent is treated by setting $a = 0$. In the present analysis, a cold-fluid guiding-center model[2] is adopted in which electron inertial effects are neglected ($m_e \to 0$), and the motion of a strongly magnetized electron fluid element is determined from

$$0 = -en_e(\underset{\sim}{x},t)\left[\underset{\sim}{E}(\underset{\sim}{x},t) + \frac{1}{c}\underset{\sim}{V}_e(\underset{\sim}{x},t) \times B_0\hat{\underset{\sim}{e}}_z\right] , \tag{2}$$

where $-e$ is the electron charge, and $\underset{\sim}{V}_e(\underset{\sim}{x},t)$ is the average flow velocity. In the electrostatic approximation, the electric field can be expressed as $\underset{\sim}{E}(\underset{\sim}{x},t) = -\nabla\phi(\underset{\sim}{x},t)$. Therefore, Eq.(2) gives

$$\underset{\sim}{V}_e(x,t) = -\frac{c}{B_0}\nabla\phi(\underset{\sim}{x},t) \times \hat{\underset{\sim}{e}}_z \tag{3}$$

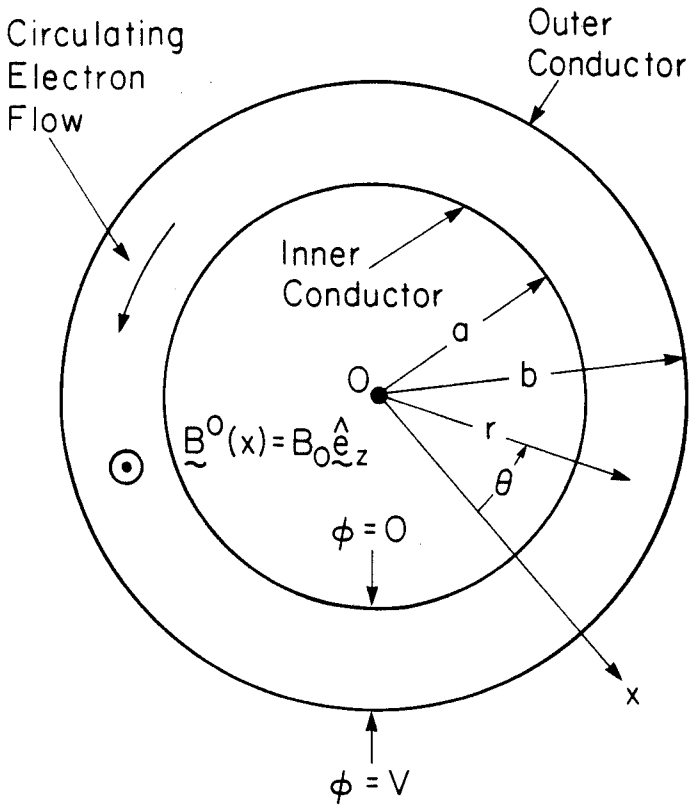

Fig. 1. A low-density nonneutral electron plasma is immersed in a strong axial magnetic field $B_0\hat{\underset{\sim}{e}}_z$ between two cylindrical conductors at r = a and r = b. In the electrostatic approximation, the perpendicular flow velocity is $\underset{\sim}{V}_e = -(c/B_0)\nabla\phi(\underset{\sim}{x},t) \times \hat{\underset{\sim}{e}}_z$.

for the perpendicular fluid motion. In cylindrical geometry, Eq.(3) reduces to

$$V_{re}(r,\theta,t) = -\frac{c}{B_0 r}\frac{\partial}{\partial\theta}\phi(r,\theta,t) \ , \tag{4}$$

$$V_{\theta e}(r,\theta,t) = \frac{c}{B_0}\frac{\partial}{\partial r}\phi(r,\theta,t) \ , \tag{5}$$

where $\partial/\partial z = 0$ is assumed. Because $\nabla \cdot \underset{\sim}{V}_e = 0$ follows from Eq.(3), the continuity equation can be expressed as

$$\left(\frac{\partial}{\partial t} - \frac{c}{B_0 r}\frac{\partial\phi}{\partial\theta}\frac{\partial}{\partial r} + \frac{c}{B_0 r}\frac{\partial\phi}{\partial r}\frac{\partial}{\partial\theta}\right) n_e(r,\theta,t) = 0 \ . \tag{6}$$

Of course, Eq.(6) must be supplemented by Poisson's equation

$$\left(\frac{1}{r}\frac{\partial}{\partial r} r \frac{\partial}{\partial r} + \frac{1}{r^2}\frac{\partial^2}{\partial\theta^2}\right)\phi(r,\theta,t) = 4\pi e n_e(r,\theta,t) \ , \tag{7}$$

which relates self-consistently the electrostatic potential $\phi(r,\theta,t)$ to the electron density $n_e(r,\theta,t)$.

Equations (6) and (7) constitute a fully nonlinear description of the two-dimensional evolution of the system in the cold-fluid guiding-center approximation with $m_e \to 0$. Although the ratio $\omega_{pe}^2/\omega_{ce}^2 = 4\pi n_e m_e c^2/B_0^2$ approaches zero in the limit of zero electron mass, note that the effective diocotron frequency defined by $\omega_D = \omega_{pe}^2/\omega_{ce} = 4\pi n_e ec/B_0$ remains finite as $m_e \to 0$. Assuming that the cylinders at $r = a$ and $r = b$ in Fig. 1 are perfect conductors, it is required that

$$E_\theta(r,\theta,t) = -\frac{1}{r}\frac{\partial}{\partial\theta}\phi(r,\theta,t) = 0, \text{ at } r = a \text{ and } r = b \ , \tag{8}$$

which corresponds to zero tangential electric field at the conducting walls. Making use of $V_{re}(r,\theta,t) = -(c/B_0 r)(\partial/\partial\theta)\phi(r,\theta,t)$, it follows from Eqs.(4) and (8) that

$$V_{re}(r,\theta,t) = 0, \text{ at } r = a \text{ and } r = b \ , \tag{9}$$

which corresponds to zero radial flow of the electron fluid at $r = a$ and $r = b$. The nonlinear equations (6) and (7) possess certain global conservation constraints[2,5] which provide important insights regarding the nonlinear evolution of the system. In particular, it is convenient to introduce the density-weighted mean-square radius of guiding-center locations defined by

$$U_r = \int_a^b dr\, r \int_0^{2\pi} d\theta\, r^2 n_e(r,\theta,t) \ , \tag{10}$$

and the generalized entropy defined by

$$U_G = \int_a^b dr r \int_0^{2\pi} d\theta\, G(n_e) \ . \tag{11}$$

Here, $G(n_e)$ is a smooth, differentiable function with $G(n_e \to 0) = 0$. Making use of Eqs.(6) and (7) and the boundary conditions in Eq.(8), it is readily shown that

$$\frac{d}{dt} U_r = 0 \ , \tag{12}$$

and

$$\frac{d}{dt} U_G = 0 \ . \tag{13}$$

That is, U_r = const. and U_G = const. are globally conserved quantities no matter how complicated the nonlinear evolution of the system described by Eqs.(6) and (7). In this regard, note that U_r = const. is a statement of the conservation of canonical angular momentum, $\int d^2x(m_e r V_{\theta e} - eB_0 r^2/2c)n_e$ = const., in the limit of zero electron mass ($m_e \to 0$).

Not only are Eqs.(12) and (13) useful conservation relations for describing the nonlinear evolution of the system, these constraint conditions can also be used to derive a sufficient condition for azimuthally symmetric equilibria $n_e^0(r)$ to be stable to small-amplitude perturbations $\delta n_e(r,\theta,t)$. In particular, for monotonically decreasing profiles with

$$\frac{1}{r}\frac{\partial}{\partial r} n_e^0(r) \leq 0 \ , \quad \text{for } a \leq r \leq b \ , \tag{14}$$

it can be shown that the density perturbation $\delta n_e(r,\theta,t)$ cannot grow without bound, and the system is linearly stable.[2,5,6] That is, Eq.(14) is a <u>sufficient condition for stability</u> to small-amplitude perturbations in the context of the cold-fluid guiding-center model based on Eqs.(6) and (7). Therefore, a <u>necessary condition for instability</u> is that the density profile $n_e^0(r)$ have a maximum at some radius $r = r_M$ intermediate between $r = a$ and $r = b$. An example of a profile subject to the diocotron instability is a sufficiently thin

annular electron layer[2,3,10] in which the inner and outer radii of the layer (at $r = r_b^-$ and $r = r_b^+$, say) are not in contact with the conductors at r = a and r = b. A smooth density profile $n_e^0(r)$ with a sufficiently large density depression $n_e^0(r = a)/n_e^0(r = r_M) < 1$ is also subject to the diocotron instability.[4]

B. Nonlinear Stationary Structures in the Rotating Frame

A thorough review of the linear properties of the diocotron instability is presented in Chapter 6 of Ref.1 and will not be repeated here. Rather, we focus on the application of Eqs.(6) and (7) to describe large-amplitude rotating structures in nonneutral plasma. As indicated earlier, one of the most ubiquitous properties of nonneutral plasma initially subject to the diocotron instability is the development of long-lived vortex structures[13] during the nonlinear evolution of the system. This has been observed experimentally in annular electron layers,[14,15] intense propagating annular electron beams,[16] nonneutral plasma columns with[17,18] and without[19-21] central conductors, and in computer simulation studies.[18] The fact that long-lived coherent structures exist in these systems for many rotation periods and thousands of cyclotron periods suggests that the nonlinear equations (6) and (7) support large-amplitude solutions which are stationary in the rotating frame.

To investigate this possibility, we look for solutions to Eqs.(6) and (7) which depend on θ and t solely through the linear combination, $\theta - \omega_r t$, where ω_r = const. is the angular rotation velocity of the disturbance. In particular, we introduce the coordinate transformation

$$\theta' = \theta - \omega_r t \ ,$$

$$r' = r \ , \qquad (15)$$

$$t' = t \ .$$

For stationary solutions $n_e(r',\theta')$ and $\phi(r',\theta')$ with $\partial/\partial t' = 0$, the continuity and Poisson equations (6) and (7) can be expressed in the rotating frame as

$$\left(-\omega_r + \frac{c}{B_0 r'}\frac{\partial\phi}{\partial r'}\right)\frac{\partial n_e}{\partial\theta'} - \frac{c}{B_0 r'}\frac{\partial\phi}{\partial\theta'}\frac{\partial n_e}{\partial r'} = 0 \ , \tag{16}$$

and

$$\left(\frac{1}{r'}\frac{\partial}{\partial r'}\, r'\, \frac{\partial}{\partial r'} + \frac{1}{r'^2}\frac{\partial^2}{\partial\theta'^2}\right)\phi = 4\pi e n_e \ . \tag{17}$$

It is convenient to introduce the stream function $\psi(r',\theta')$ defined by

$$\psi(r',\theta') = \frac{c}{B_0}\,\phi(r',\theta') - \frac{1}{2}\,\omega_r r'^2 \ . \tag{18}$$

Equations (16) and (17) then become

$$\frac{\partial\psi}{\partial r'}\frac{\partial n_e}{\partial\theta'} - \frac{\partial\psi}{\partial\theta'}\frac{\partial n_e}{\partial r'} = 0 \ , \tag{19}$$

$$\left(\frac{1}{r'}\frac{\partial}{\partial r'}\, r'\, \frac{\partial}{\partial r'} + \frac{1}{r'^2}\frac{\partial^2}{\partial\theta'^2}\right)\psi = \frac{4\pi e c}{B_0}\, n_e - 2\omega_r \ . \tag{20}$$

Note that introducing the term $-\omega_r r'^2/2$ in the definition of the stream function $\psi(r',\theta')$ in Eq.(18) is equivalent to reducing the density by a constant amount $(B_0/2\pi ec)\omega_r$ in Poisson's equation (20).

The general stationary solution to the continuity equation (19) in the rotating frame is

$$n_e(r',\theta') = n_e[\psi(r',\theta')] \ , \tag{21}$$

where $n_e(\psi)$ is a (yet unspecified) function of ψ. Substituting Eq.(21) into Eq.(20) then gives

$$\left(\frac{1}{r'}\frac{\partial}{\partial r'}\, r'\, \frac{\partial}{\partial r'} + \frac{1}{r'^2}\frac{\partial^2}{\partial\theta'^2}\right)\psi = \frac{4\pi e c}{B_0}\, n_e(\psi) - 2\omega_r \ . \tag{22}$$

It is evident from Eq.(22) that there is considerable latitude in determining stationary solutions that depend on both r' and θ' in the rotating frame. Once the functional form of $n_e(\psi)$ is specified,

then Eq.(22) is solved numerically or analytically, as appropriate, for the stream function $\psi(r',\theta) = c\phi(r',\theta)/B_0 - \omega_r r'^2/2$. The boundary conditions consistent with zero tangential electric field at the perfectly conducting walls in Fig. 1 are given by [see Eq.(8)]

$$\left[\frac{\partial}{\partial\theta'}\psi(r',\theta)\right]_{r'=a} = 0 = \left[\frac{\partial}{\partial\theta'}\psi(r',\theta')\right]_{r'=b} . \tag{23}$$

In addition, it is assumed that the inner and outer conductors are maintained at a constant potential difference corresponding to $\phi(r' = a,\theta) = 0$ and $\phi(r' = b,\theta) = V$, or equivalently,

$$\begin{aligned} \psi(r' = a,\theta') &= -\frac{1}{2}\omega_r a^2 , \\ \psi(r' = b,\theta') &= \frac{cV}{B_0} - \frac{1}{2}\omega_r b^2 , \end{aligned} \tag{24}$$

where V is the potential difference.

C. Example of Large-Amplitude Vortex Solutions

Depending on the choice of $n_e(\psi)$, there is considerable latitude in determining stationary solutions to Eq.(22) that depend on both r' and θ' in the rotating frame. In this section, we consider a simple example which is analytically tractable and corresponds to a large-amplitude vortex solution. In particular, it is assumed that $n_e(\psi)$ is specified by the linear function

$$n_e(\psi) = \hat{n}_e(C_0 + C_1\psi) , \tag{25}$$

where C_0 and C_1 are constants, and $\hat{n}_e$ = const. is a measure of the characteristic electron density in the interval $a \leq r \leq b$. Introducing the effective diocotron frequency ω_D = const. defined by

$$\omega_D = \frac{4\pi\hat{n}_e ec}{B_0} , \tag{26}$$

Poisson's equation (22) becomes

$$\left(\frac{1}{r'}\frac{\partial}{\partial r'}r'\frac{\partial}{\partial r'}+\frac{1}{r'^2}\frac{\partial^2}{\partial\theta'^2}\right)\psi=\omega_D C_0-2\omega_r+\omega_D C_1\psi\ . \tag{27}$$

The (linear) differential equation (27) can be solved exactly for $\psi(r',\theta')$ subject to the boundary conditions in Eqs.(23) and (24).

We examine solutions to Eq.(27) of the form

$$\psi(r',\theta')=\psi_0(r')+a_\ell\psi_\ell(r')\cos(\ell\theta')\ , \tag{28}$$

where $\ell\neq 0$ is an integer and a_ℓ is a constant amplitude factor. Substituting Eq.(28) into Eq.(27) then gives

$$\left(\frac{1}{r'}\frac{\partial}{\partial r'}r'\frac{\partial}{\partial r'}+k^2\right)\psi_0(r')=\omega_D C_0-2\omega_r\ , \tag{29}$$

and

$$\left(\frac{1}{r'}\frac{\partial}{\partial r'}r'\frac{\partial}{\partial r'}+k^2-\frac{\ell^2}{r'^2}\right)\psi_\ell(r')=0\ , \tag{30}$$

where $k^2\equiv-\omega_D C_1>0$ is assumed. The solutions to Eqs.(29) and (30) in the interval $a\leq r\leq b$ are linear combinations of $J_0(kr')$ and $N_0(kr')$, and $J_\ell(kr')$ and $N_\ell(kr')$, respectively. Here, $J_\ell(x)$ is the Bessel function of the first kind of order ℓ, and $N_\ell(x)$ is the Neumann function of order ℓ. For present purposes, we also consider the class of solutions in which the electron density is equal to zero at the outer conductor, i.e., $n_e(r'=b,\theta')=\hat{n}_e[C_0+C_1\psi(r'=b,\theta')]=0$. Making use of $\psi(r'=b,\theta')=cV/B_0-\omega_r b^2/2$ [Eq.(24)], this condition relates the constants C_0 and $C_1=-k^2/\omega_D$ by

$$C_0=-C_1\left(\frac{cV}{B_0}-\frac{1}{2}\omega_r b^2\right)\ . \tag{31}$$

We solve Eqs.(29) and (30) for $\psi_0(r')$ and $\psi_\ell(r')$ and substitute into Eq.(28). Enforcing the boundary conditions in Eqs.(23) and (24) then gives the desired solutions for the electrostatic potential $c\phi(r',\theta')/B_0=\psi(r',\theta')+\omega_r r'^2/2$ and the electron density

$n_e(r',\theta') = n_e[C_0 + C_1\psi(r',\theta')]$. In laboratory-frame variables (r,θ,t), some straightforward algebra gives

$$\frac{c}{B_0}\phi(r,\theta,t) = \left[\frac{cV}{B_0} - \frac{\omega_r}{2}\left(b^2 - r^2 + \frac{4}{k^2}\right)\right]$$

$$- \left[\frac{cV}{B_0} - \frac{\omega_r}{2}\left(b^2 - a^2 + \frac{4}{k^2}\right)\right]\left[\frac{J_0(kb)N_0(kr) - N_0(kb)J_0(kr)}{J_0(kb)N_0(ka) - N_0(kb)J_0(ka)}\right]$$

$$+ \frac{2\omega_r}{k^2}\left[\frac{N_0(ka)J_0(kr) - J_0(ka)N_0(kr)}{N_0(ka)J_0(kb) - J_0(ka)N_0(kb)}\right] \qquad (32)$$

$$+ a_\ell\left[J_\ell(kr) - \frac{J_\ell(ka)}{N_\ell(ka)}N_\ell(kr)\right]\cos[\ell(\theta - \omega_r t)] \ ,$$

and

$$n_e(r,\theta,t) = \hat{n}_e\frac{2\omega_r}{\omega_D}\left[1 - \frac{N_0(ka)J_0(kr) - J_0(ka)N_0(kr)}{N_0(ka)J_0(kb) - J_0(ka)N_0(kb)}\right]$$

$$+ \hat{n}_e\frac{k^2}{\omega_D}\left[\frac{cV}{B_0} - \frac{\omega_r}{2}\left(b^2 - a^2 + \frac{4}{k^2}\right)\right]\left[\frac{J_0(kb)N_0(kr) - N_0(kb)J_0(kr)}{J_0(kb)N_0(ka) - N_0(kb)J_0(ka)}\right] \qquad (33)$$

$$- \hat{n}_e\frac{k^2 a_\ell}{\omega_D}\left[J_\ell(kr) - \frac{J_\ell(ka)}{N_\ell(ka)}N_\ell(kr)\right]\cos[\ell(\theta - \omega_r t)] \ .$$

Here, a_ℓ is the constant amplitude factor, $\ell = 1,2,3,\cdots$ is an integer, and the parameter k is chosen to satisfy

$$J_\ell(kb)N_\ell(ka) - J_\ell(ka)N_\ell(kb) = 0 \ . \qquad (34)$$

From Eqs.(32) and (34), it follows trivially that the electrostatic potential $\phi(r,\theta,t)$ satisfies the boundary conditions $[\phi]_{r=a} = 0$, $[\phi]_{r=b} = V$, $[\partial\phi/\partial\theta]_{r=a} = 0$, and $[\partial\phi/\partial\theta]_{r=b} = 0$, consistent with Eqs.(23) and (24). In addition, from Eqs.(33) and (34), the electron density is equal to zero at the outer conductor in Fig. 1,

i.e., $n_e(r = b,\theta,t) = 0$. On the other hand, evaluating Eq.(33) at $r = a$ gives the steady value $n_e(r = a,\theta,t) = n_e(a)$, where

$$n_e(a) \equiv \hat{n}_e \frac{k^2}{\omega_D}\left[\frac{cV}{B_0} - \frac{\omega_r}{2}(b^2 - a^2)\right] . \tag{35}$$

Evidently, Eqs.(32) and (33) describe structured potential and density profiles which rotate azimuthally about the z-axis in Fig. 1 with angular velocity ω_r = const. Note that the profiles are stationary (independent of time) in the rotating frame. Furthermore, for specified integer ℓ, the profiles described by Eqs.(32) and (33) have azimuthal periodicity $2\pi/\ell$ in the rotating frame. In particular, insofar as Eqs.(32) and (33) represent a coherent vortex structure, $\ell = 1$ corresponds to one vortex, $\ell = 2$ corresponds to two vortices, etc. As a further important point, for the solution in Eq.(33) to be physically acceptable, it is required that the electron density profile satisfy

$$n_e(r,\theta,t) \geq 0 \tag{36}$$

in the entire region $a \leq r \leq b$ and $0 \leq \theta \leq 2\pi$ between the conducting cylinders in Fig. 1. This places restrictions on the allowed values of the dimensionless parameters kb, ω_r/ω_D and $k^2cV/\omega_D B_0$, and the dimensionless amplitude $k^2 a_\ell/\omega_D$ of the oscillatory (θ-dependent) term in Eq.(33).

Figures 2-5 illustrate properties of the solutions for ϕ and n_e in Eqs.(32) and (33) for disturbances with azimuthal mode number $\ell = 1$ (Figs. 2 and 3) and $\ell = 2$ (Figs. 4 and 5). Because the structures in Eqs.(32) and (33) rotate azimuthally about the z-axis with angular velocity ω_r = const., the information in Figs. 2-5 is displayed at time $t = 0$ without loss of generality.

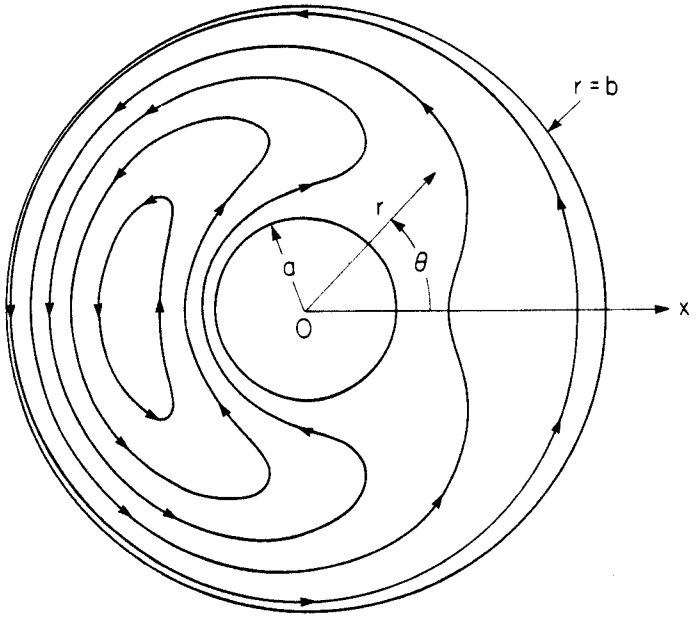

Fig. 2. Plots of the equipotential contours $\phi(r,\theta,t = 0) = \text{const.}$ calculated from Eq.(32) for $\ell = 1$ and the system parameters in Eq.(37). The arrows indicate the direction of the circulating electron flow $\underset{\sim}{V}_e = -(c/B_0)\nabla\phi \times \hat{\underset{\sim}{e}}_z$.

The choice of system parameters in Figs. 2 and 3 corresponds to $\ell = 1$ and

$$\frac{a}{b} = 0.3 \ , \quad kb = 4.7058 \ , \quad \frac{\omega_r}{\omega_D} = 0.2 \ , \qquad (37)$$

$$\frac{k^2 cV}{\omega_D B_0} = 2.2144 \ , \quad \frac{k^2 a_\ell}{\omega_D} = 4.4289 \ .$$

Here, $kb = 4.7058$ is the first zero of Eq.(34) for $\ell = 1$ and $a/b = 0.3$. Figure 2 shows plots of the equipotential contours, $\phi(r,\theta,t = 0) = \text{const.}$, calculated from Eqs.(32) and (37). From Eqs.(3)-(5), the flow velocity $\underset{\sim}{V}_e = -(c/B_0)\nabla\phi \times \hat{\underset{\sim}{e}}_z$ is tangential to the contours $\phi = \text{const.}$ Therefore, the local flow velocity

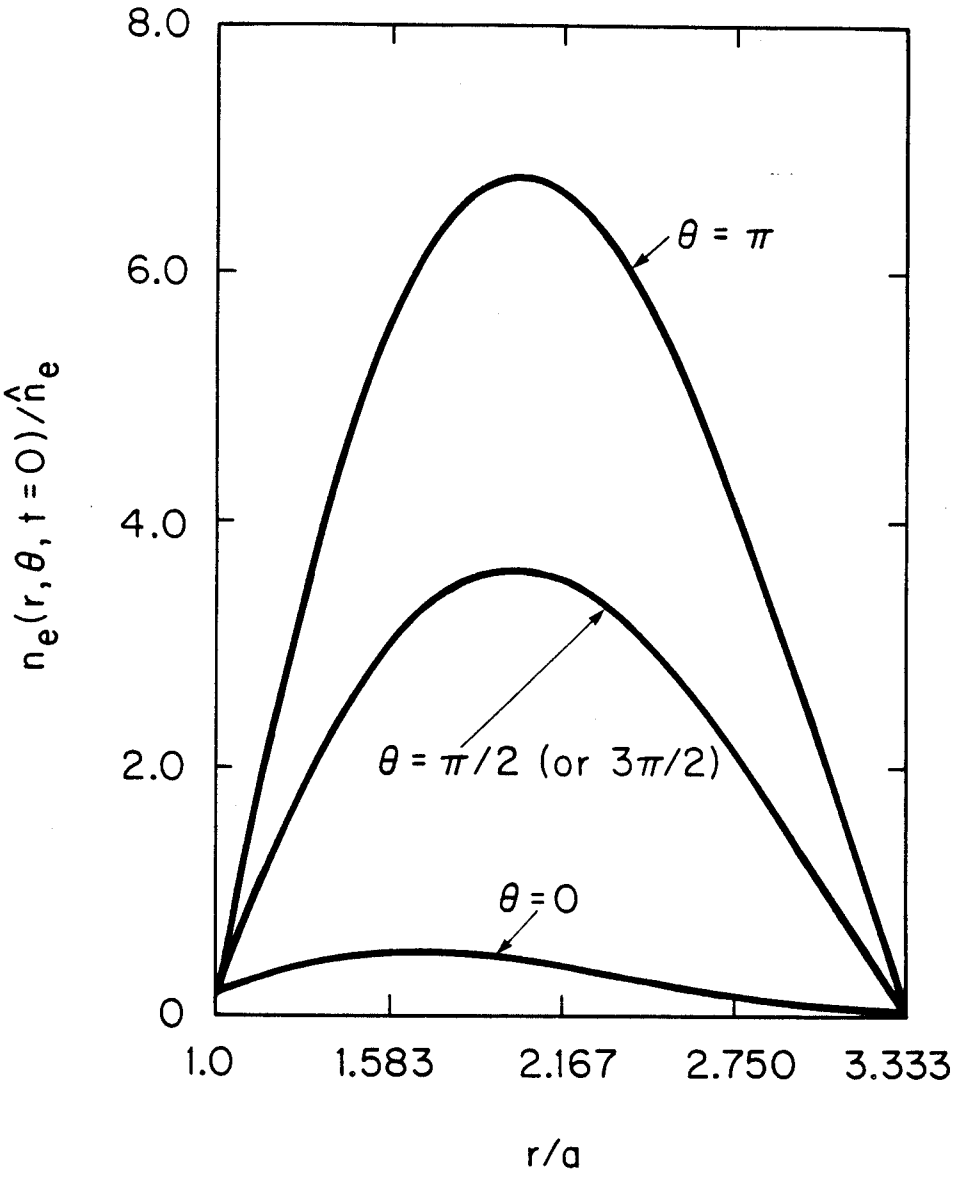

Fig. 3. Plots versus r/a of the density profile $n_e(r,\theta,t = 0)$ calculated from Eq.(33) for $\ell = 1$ and values of θ corresponding to $\theta = 0$, $\theta = \pi/2$ (or $\theta = 3\pi/2$), and $\theta = \pi$. The choice of system parameters is the same as in Eq.(37) and Fig. 2.

circulates in the direction indicated by the arrows in Fig. 2. Evidently, the structure centered around $\theta = \pi$ in Fig. 2 corresponds to a large-amplitude vortex localized between $r = a$ and $r = b$. The corresponding radial dependence of the density profile $n_e(r,\theta,t = 0)$ calculated from Eqs.(33) and (37) is illustrated in Fig. 3 for $\theta = 0$, $\theta = \pi/2$ (or $\theta = 3\pi/2$), and $\theta = \pi$. It is evident from Fig. 3 that the density compression is large at the center of the vortex. Note also from Eq.(33) that the profile for $n_e(r,\theta = \pi/2,\ t = 0)$ plotted in Fig. 3 is the same as the azimuthally averaged density profile

$$\langle n_e\rangle(r,t = 0) = \frac{1}{2\pi}\int_0^{2\pi} d\theta\, n_e(r,\theta,t = 0) \ .$$

The choice of system parameters in Figs. 4 and 5 corresponds to $\ell = 2$ and

$$\frac{a}{b} = 0.3 \ , \quad kb = 5.4702 \ , \quad \frac{\omega_r}{\omega_D} = 0.4 \ , \qquad \frac{k^2 cV}{\omega_D B_0} = 5.9847 \ , \quad \frac{k^2 a_\ell}{\omega_D} = 2.9923 \ . \tag{38}$$

Here, $kb = 5.4702$ is the first zero of Eq.(34) for $\ell = 2$ and $a/b = 0.3$. Figure 4 shows plots of the equipotential contours, $\phi(r,\theta,t = 0) = \text{const.}$, calculated from Eqs.(32) and (38). The direction of the local flow velocity is indicated by the arrows in Fig. 4. Evidently, for $\ell = 2$, there are two large-amplitude vortices centered around $\theta = \pi/2$ and $\theta = 3\pi/2$. Moreover, the density compression is large at the center of the vortices. This is evident from Fig. 5 which shows the radial dependence of the density profile $n_e(r,\theta,t = 0)$ calculated from Eqs.(33) and (38) for $\theta = 0$ (or $\theta = \pi$) and $\theta = \pi/2$ (or $\theta = 3\pi/2$).

To summarize, Figs. 2-5 and the analysis in Secs. II.B and II.C demonstrate that a simple cold-fluid guiding-center model of a low-density nonneutral plasma supports large-amplitude vortex solutions which are stationary in the rotating frame. What is most striking

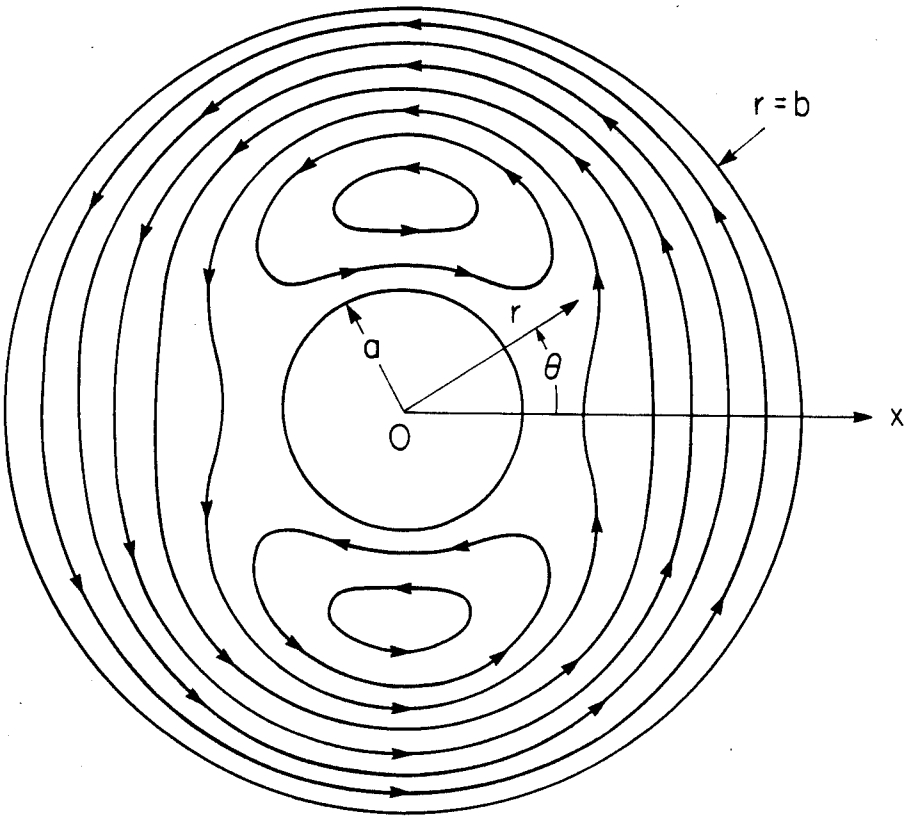

Fig. 4. Plots of the equipotential contours $\phi(r,\theta,t = 0) = \text{const.}$ calculated from Eq.(32) for $\ell = 2$ and the choice of system parameters in Eq.(38). The arrows indicate the direction of the circulating electron flow $\underset{\sim}{V}_e = -(c/B_0)\nabla\phi \times \hat{\underset{\sim}{e}}_z$.

is that the coherent structures described by Eqs.(32) and (33) are very rich in detail for the case in which $n_e(\psi)$ is assumed to have a simple linear dependence on ψ with $n_e(\psi) = \hat{n}_e(C_0 + C_1\psi)$. Even more structure would be present in the nonlinear case where a quadratic term is included with $n_e(\psi) = \hat{n}_e(C_0 + C_1\psi + C_2\psi^2)$. Finally, it should be emphasized that the present analysis addresses only the existence of coherent structures which are stationary in the rotating frame. The question of accessibility of such solutions from prescribed initial conditions $n_e(r,\theta,t = 0)$ is not addressed by the present analysis, although the constants ω_r/ω_D, k^2a_ℓ/ω_D, etc., occurring in Eqs.(32) and (33) can be related to the initial

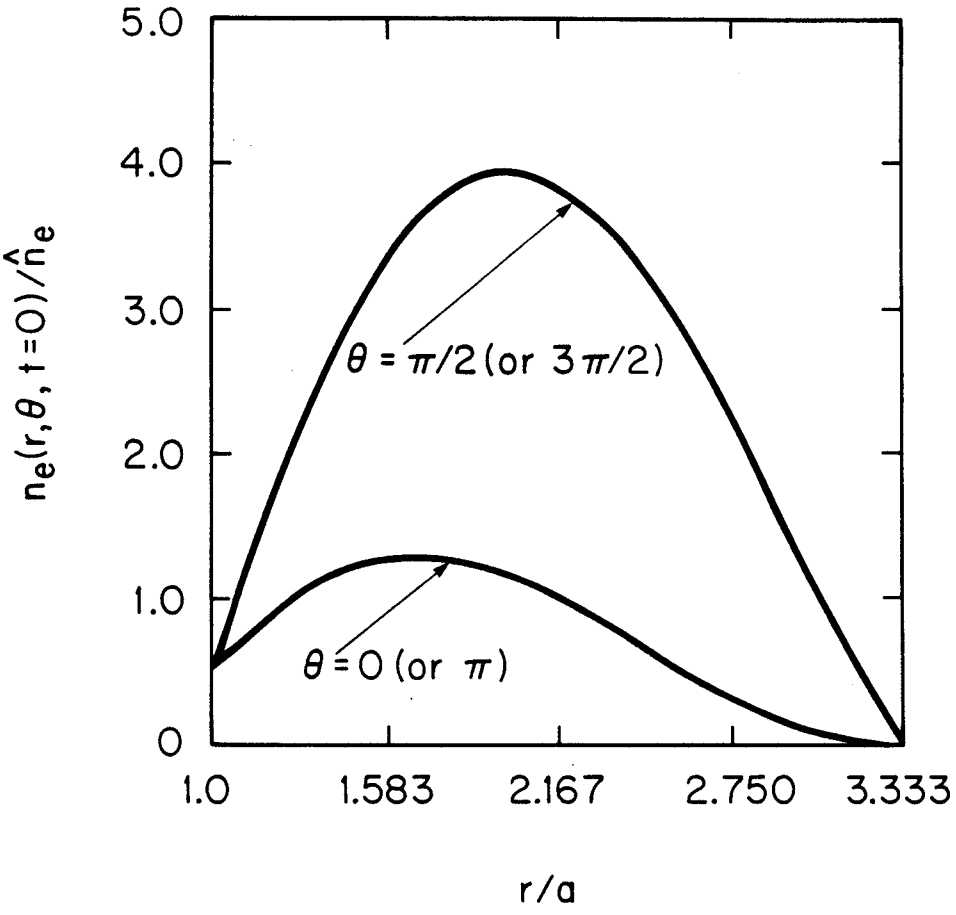

Fig. 5. Plots versus r/a of the density profile $n_e(r,\theta,t = 0)$ calculated from Eq.(33) for $\ell = 2$ and values of θ corresponding to $\theta = 0$ (or $\theta = \pi$), and $\theta = \pi/2$ (or $\theta = 3\pi/2$). The choice of system parameters is the same as in Eq.(38) and Fig. 4.

conditions by the global conservation constraints in Eqs.(10) and (11). In addition, the stability of such large-amplitude structures requires an analysis of the evolution of small-amplitude perturbations, δn_e and $\delta\phi$, about the solutions in Eqs.(32) and (33).

III. COMPUTER SIMULATION OF THE NONLINEAR ELECTRODYNAMICS OF RELATIVISTIC MAGNETRONS

In relativistic magnetrons,[22-30] pulsed high-voltage diodes (operating in the several hundred kV to MV range, say) are used to generate microwaves at gigawatt power levels. Although magnetrons are widely used as microwave sources, a fundamental understanding of the underlying interaction physics is still being developed,[31] particularly in the nonlinear regime. Much of the theoretical challenge in describing multiresonator magnetron operation arises from the complexity introduced by the corrugated anode boundary[30] and the fact that the electrons emitted from the cathode interact with the electromagnetic waves in the anode-cathode gap in a highly nonlinear way. This is manifest through strong azimuthal bunching of the electrons and the formation of a large-amplitude "spoke" structure in the circulating electron density. In this regard, computer simulation studies[32-35] provide a particularly valuable approach to analyze the interaction physics and nonlinear electrodynamics in magnetrons. In this section, we summarize recent computer simulations[35] of the multiresonator A6 magnetron configuration of Palevsky and Bekefi[26] using the two-dimensional ($\partial/\partial z = 0$) particle-in-cell code MAGIC.[36]

A. Simulation Model and A6 Magnetron Configuration

The MAGIC simulation code includes cylindrical effects, and relativistic and electromagnetic effects in a fully self-consistent manner. Unlike previous computer simulations,[32-34] the magnetron oscillations in the present studies[35] are excited from noise, i.e., without preinjection of a finite-amplitude rf signal or preferential excitation of 2π-mode or π-mode oscillations. In addition, the present simulations[35] are carried out in cylindrical rather than planar[32,33] magnetron geometry. Figure 6 shows the cross section of the A6 magnetron diode.[26] The cold, field-emission, graphite cathode is located at radius $a = 1.58$ cm. The inside radius of the anode block is $b = 2.11$ cm, and six vane-type resonators with outer radius $d = 4.11$ cm are used, with angle $\psi = 20°$ subtended by the resonators on axis. The axial magnetic field $B_f\hat{e}_z$ prior to

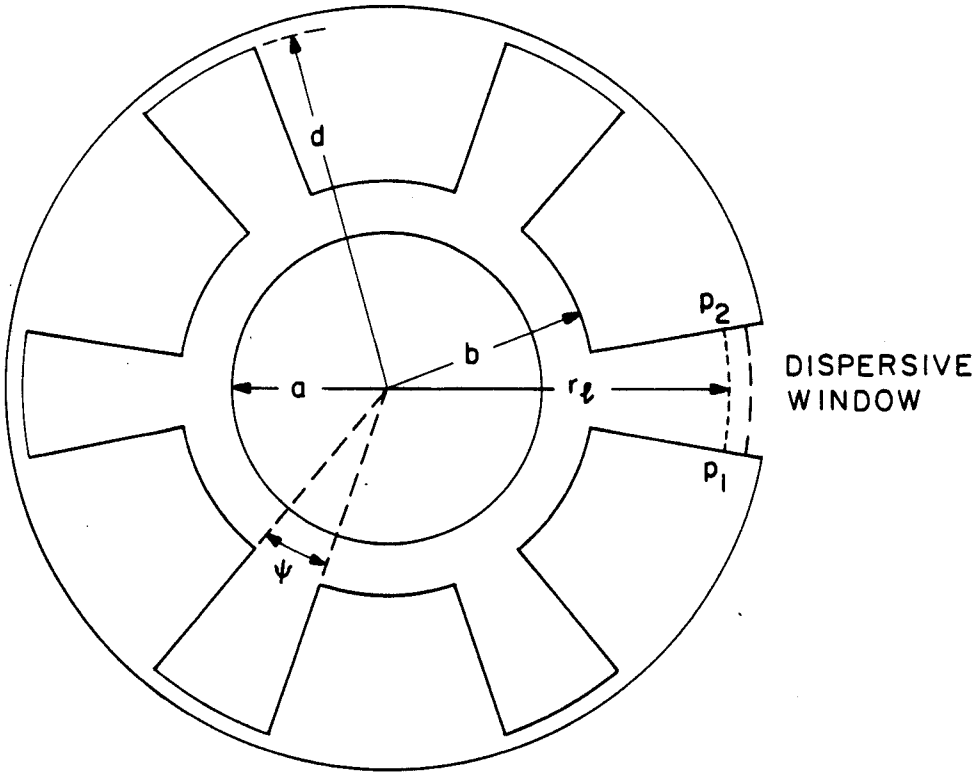

Fig. 6. Schematic of the A6 magnetron used in the computer simulations. The rf power is partially absorbed by the dispersive window (dashed line) located at r = d = 4.11 cm in the open resonator. Here, a = 1.58 cm, b = 2.11 cm, d = 4.11 cm, and $\psi = 20°$.

formation of the circulating electron layer (the so-called "fill" magnetic field) ranges from 4-10 kG in typical operation.[26] The axial length of the anode block is L = 7.2 cm, and the operating voltage is 300-400 kV. The annular interaction space between r = a and r = b together with the periodically-spaced vanes can be viewed as a coaxial microwave resonator. For transverse electric (TE) modes with $\delta\underset{\sim}{E}$ perpendicular to $B_f\hat{e}_z$ and $\delta\underset{\sim}{B}$ parallel to $B_f\hat{e}_z$, the vacuum electric field pattern is such that δE_θ is in phase in adjacent resonators for the 2π mode, whereas δE_θ is out of phase in adjacent resonators for the π mode.

In circumstances where the magnetically insulated electron flow is described by an ideal Brillouin flow model,[22] the cylindrical

expressions for the Hull cut-off voltage V_H and the Buneman-Hartree threshold voltage V_{BH} can be expressed relativistically as[31]

$$\frac{eV_H}{m_e c^2} = \left[1 + \frac{e^2 B_f^2}{m_e^2 c^4}\left(\frac{b^2 - a^2}{2b}\right)^2\right]^{1/2} - 1 , \tag{39}$$

and

$$\frac{eV_{BH}}{m_e c^2} = \frac{eB_f}{m_e c^2}\left(\frac{b^2 - a^2}{2b}\right)\beta_p - \left[1 - \left(1 - \beta_p^2\right)^{1/2}\right] . \tag{40}$$

Here, $\beta_p c$ is the phase velocity of the electromagnetic wave excited in the interaction region. For steady Brillouin flow in a cylindrical diode with specified fill field B_f, the inequality $V < V_H$ is required to assure magnetic insulation of the azimuthal flow from contact with the anode at $r = b$, whereas $V > V_{BH}$ is required for interaction of the outermost electrons with the electromagnetic wave field.

In the simulations, Maxwell's equations and the particle orbit equations are solved relativistically and electromagnetically, using (typically) more than 3000 macroparticles and a nonuniform, two-dimensional grid consisting of approximately 3000 cells. When a voltage $V_D(t)$ is applied across the diode shown in Fig. 6, the electrons are emitted from the cathode through a space-charge-limited emission process in which the instantaneous electric field normal to the cathode surface vanishes. The radial momenta of the emitted electrons are randomly distributed from 0 to 0.02 $m_e c$. On the other hand, electrons are absorbed by the anode or cathode whenever they strike the surface. The simulations are carried out with one open resonator, which is modeled by a dispersive window placed along the dashed line in Fig. 6 at $r = d = 4.11$ cm. At the window, the boundary condition is such that most of the electromagnetic wave energy is absorbed, while a small fraction of the wave energy is reflected back into the cavity. Such a window yields a finite Q factor for the system. The rf power output is determined from the net flow of electromagnetic energy expressed as an area-integral of the Poynting flux over the window surface shown in Fig. 6.

A quasi-static model is used in the simulations to describe the high-voltage pulse applied to the diode. In such a model, the diode voltage is given by $V_D(t) = Z(t)V_0(t)/[Z_0 + Z(t)]$, where $V_0(t)$ is the voltage pulse provided by the power supply, Z_0 = const. is the impedance of the power supply, and $Z(t)$ is the magnetron impedance. In the simulations, the voltage pulse $V_0(t)$ is assumed to have the form

$$V_0(t) = \begin{cases} 0 , & t < 0 , \\ (t/t_0)V_m , & 0 \le t < t_0 , \\ V_m , & t \ge t_0 , \end{cases} \tag{41}$$

where t_0 and V_m are the rise time and maximum value of the voltage pulse, respectively. The rise time assumed in the simulations is t_0 = 4.0 ns, corresponding to the experimental value.[26] Although the applied high-voltage pulse in the simulations is described by Eq.(41), it should be emphasized that all extraordinary-mode rf excitations ($\delta\underset{\sim}{B} = \delta B_z \hat{\underset{\sim}{e}}_z$ and $\delta\underset{\sim}{E} = \delta E_r \hat{\underset{\sim}{e}}_r + \delta E_\theta \hat{\underset{\sim}{e}}_\theta$) are treated fully electromagnetically.

B. Simulation Results

Typical numerical results are presented in Figs. 7-10 for the case of an ideal power supply where $Z_0 = 0$ and $V_D(t) = V_0(t)$.

Figure 7(a) shows the time history of the integrated rf field profile

$$V_\theta(t) = \int_{P_1}^{P_2} d\theta \, r_\ell \, \delta E_\theta(r_\ell , \theta, t) \tag{42}$$

for the choice of system parameters B_f = 7.2 kG, V_m = 350 kV and t_0 = 4.0 ns. In Fig. 7(b), the Fourier transform of the signal in Fig. 7(a) is plotted versus frequency f. Here, the integration path corresponds to the dotted line in Fig. 6 from P_1 to P_2 at $r = r_\ell$ = 3.7 cm. In Fig. 7(a), the nonlinear saturation of the magnetron oscillations occurs at $t \simeq 10$ ns, where the ratio of the saturated amplitude $V_{\theta s}$ and the applied diode voltage $V_D = V_m$ is $V_{\theta s}/V_D \simeq 0.85$.

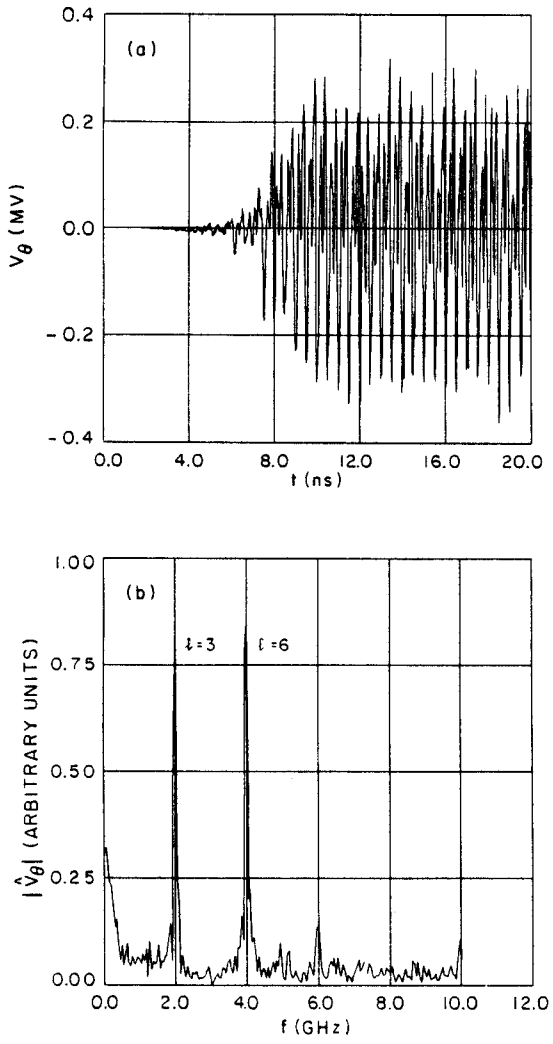

Fig. 7. Shown in Fig. 7(a) is the time history of the integrated rf field profile $V_\theta(t) = \int_{P_1}^{P_2} d\theta\, r_\ell\, \delta E_\theta(r_\ell, \theta, t)$ obtained in the simulations at radius $r = r_\ell = 3.7$ cm in the open resonator for the choice of system parameters B_f = 7.2 kG, V_m = 350 kV, t_0 = 4.0 ns, and Z_0 = 0. Figure 7(b) shows the magnitude of the Fourier transform, $|\hat{V}_\theta(f)|$, of the signal in Fig. 7(a). The two distinct peaks at f = 2.0 GHz and f = 4.0 GHz correspond to π-mode (ℓ = 3) and 2π-mode (ℓ = 6) oscillations, respectively.

In Fig. 7(b), the two distinct peaks at the frequencies f = 2.0 GHz and f = 4.0 GHz correspond to π-mode and 2π-mode oscillations, respectively. The 2π-mode oscillation frequency f = 4.0 GHz is 14% lower than the frequency f = 4.55 GHz observed in the experiment,[26] which may be due to the absence of finite-axial-length effects in the simulations (where $\partial/\partial z = 0$ is assumed). Although both the π-mode and 2π-mode excitations have nearly the same wave amplitudes in Fig. 7(b), the (higher frequency) 2π mode delivers more rf power than the π mode.

By evaluating the area-integral of the outward Poynting flux $(c/4\pi)\delta E_\theta \delta B_z$ over the surface of the dispersive window at r = d = 4.11 cm in Fig. 6, the peak rf power output in the simulations is calculated for various values of the applied magnetic field B_f. The dependence of the normalized rf power on magnetic field is shown in Fig. 8. Here, the dots correspond to the experimental values,[26] and the triangles are obtained from the simulations with $Z_0 = 0$. In Fig. 8, the normalization is chosen such that the maximum values of the rf power in both the simulations and the experiment are equal to unity. The actual value of the maximum rf output per unit axial length in the simulations is 4.3 GW/m. For the A6 magnetron, with axial length L = 7.2 cm, this corresponds to P = 0.3 GW, which is somewhat less than the maximum rf power P = 0.45 GW measured in the experiment.[26] (The values of power quoted here are rms values.) Apart from a constant scale factor, it is evident from Fig. 8 that the simulations are in excellent agreement with the experimental results. The difference in scale factor may be due to the fact that a larger fraction of the rf power in the simulations is reflected back into the cavity, and the effective Q-value in the simulations (Q ~ 100) is greater than in the experiment (Q ~ 20-40). As B_f is decreased below 6 kG, crossing the Hull cut-off curve[22] at a diode voltage corresponding to V_D = 350 kV, it is found that the 5π/3-mode ($\ell = 5$) becomes the dominant rf excitation in the simulations.

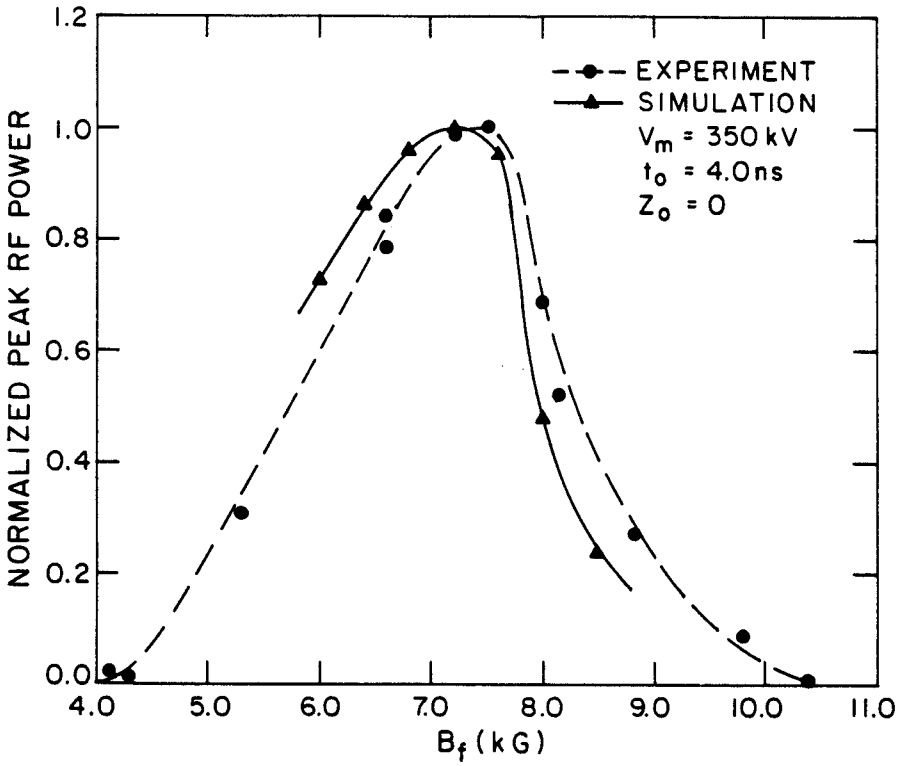

Fig. 8. Plots of the normalized peak rf power versus the applied magnetic field B_f. The dots correspond to the experimental results [A. Palevsky and G. Bekefi, Phys. Fluids 22, 986 (1979)], and the triangles correspond to the simulation results for V_m = 350 kV, t_0 = 4.0 ns, and Z_0 = 0. The maximum rf power is 0.45 GW per open port in the experiment, and 0.3 GW in the simulations.

Figure 9 shows radial plots of the charge density,

$$e\langle n_e\rangle(r,t) = \frac{1}{2\pi}\int_0^{2\pi} e n_e(r,\theta,t)\,d\theta \,, \tag{43}$$

averaged over the azimuthal angle θ, at several instants of time for the same values of system parameters as in Fig. 7. In Fig. 9, the outer radius of the electron layer [$r = r_b(t)$], designated by the

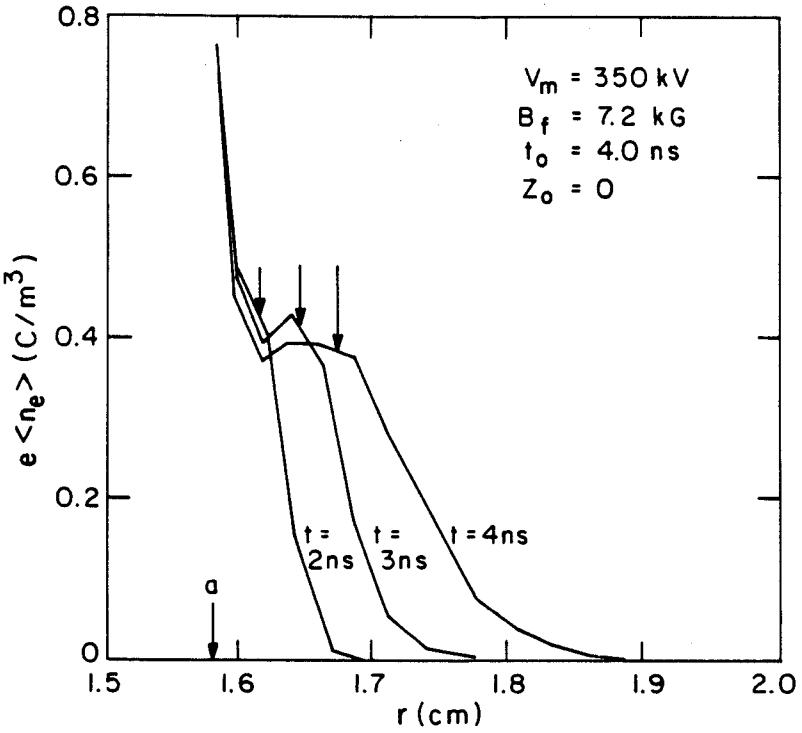

Fig. 9. Plots of the azimuthally averaged charge density $e\langle n_e\rangle(r,t)$ versus radial distance r obtained in the simulations at times t = 2.0, 3.0, 4.0 ns for system parameters the same as in Fig. 7. Here, the arrows designate the location of the outer envelope ($r = r_b$) of the electron layer calculated from a simple Brillouin flow model.

arrows, is calculated from a simple Brillouin flow model[22] for B_f = 7.2 kG and diode voltages $V_D(t) = 0.5\ V_m$, $0.75\ V_m$, $1.0\ V_m$, corresponding to t = 2.0, 3.0, 4.0 ns. It is clear from Fig. 9 that a substantial fraction of the electrons occupy the region between $r = r_b$ and the anode (r = b). The existence of a long tail in the electron density profile indicates that the electron flow differs significantly from the ideal Brillouin flow model. For the A6 magnetron operating at $V_m \simeq 350$ kV, cylindrical and relativistic effects are relatively mild. For example, at $t = t_0 = 4.0$ ns, the

layer aspect ratio is $A = a/(r_b - a) \simeq 1.15$. We define the local self-field parameter $s_e(r)$ by

$$s_e(r) = \frac{\omega_{pe}^2(r)/\gamma_e(r)}{\omega_{ce}^2(r)/\gamma_e^2(r)} , \tag{44}$$

where $\omega_{ce}(r) = e\langle B_z\rangle/m_e c$ is the nonrelativistic cyclotron frequency, $\omega_{pe}^2(r) = 4\pi\langle n_e\rangle e^2/m_e$ is the nonrelativistic plasma frequency-squared, and $\gamma_e(r) = (1 - V_{\theta e}^2/c^2)^{-1/2}$ is the relativistic mass factor of an electron fluid element. Under ideal Brillouin flow conditions,[22] the self-field parameter satisfies $s_e = 1$ (in the planar approximation). In the simulations, however, it is found that $s_e(r)$ decreases considerably as r increases from $r = a$ to $r = r_b$ and beyond. For example, at $t = t_0 = 4.0$ ns in Fig. 9, the self-field parameter decreases from $s_e(r = a) \simeq 1$ at the cathode, to $s_e(r = r_b) \simeq 0.5$ at $r = r_b$.

Although the azimuthal bunching of the electrons is relatively small for times up to 4 ns, by $t \simeq 6$ ns the system begins to enter a nonlinear regime characterized by large-amplitude spoke formation. Highly developed spokes are evident in Fig. 10(b) which shows density contour plots at $t = 8$ ns for the choice of system parameters $B_f = 7.2$ kG, $V_m = 350$ kV and $t_0 = 4$ ns (similar to the conditions in Fig. 7, and the maximum power simulation point in Fig. 8). As the system evolves, the spokes rotate as coherent nonlinear structures in the azimuthal direction for hundreds of electron cyclotron periods. In addition, by $t = 7$ ns, there is current flow from the cathode to the anode. At saturation, which occurs at $t \simeq 10$ ns, the time-averaged diode current per unit axial length is $I_D \simeq 100$ kA/m, and the amplitude of the integrated rf field profile $\int_a^b dr\, \delta E_r(r,\theta,t)$ is comparable with the diode voltage $V_D \simeq V_m = 350$ kV.

To summarize, with regard to the dependence of rf power on magnetic field, the simulation results are in excellent agreement with experiment (within a constant scale factor). Also, in terms of rf power output, the simulations confirm that the A6 magnetron oscillates preferentially in the 2π mode. In the preoscillation regime, it is found that the electron flow differs substantially from

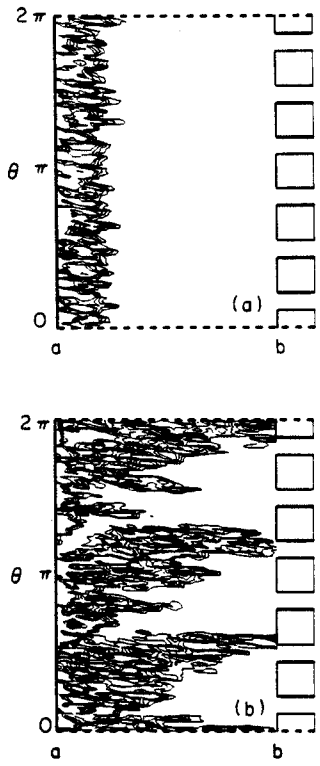

Fig. 10. Density contour plots for $n_e(r,\theta,t)$ obtained in the simulations at (a) t = 3.0 ns and (b) t = 8.0 ns for the same system parameters as in Fig. 7.

Brillouin flow conditions. In the nonlinear regime, the saturation is dominated by the formation of a large-amplitude spoke structure in the circulating electron density. The simulations also show that the magnetron performance and rf power generation are degraded when the impedance Z_0 of the external power supply is increased (in agreement with experiment) from the ideal value $Z_0 = 0$. As a general conclusion, based on the results presented here, it is expected that the MAGIC simulation code can be used as an effective tool for developing a fundamental understanding of the large-amplitude spoke dynamics and saturation in magnetrons, as well as for experimental magnetron design.

IV. REFERENCES

1. R.C. Davidson, Physics of Nonneutral Plasmas (Addison-Wesley, Reading, Massachusetts, 1990).
2. Ibid., Chapter 6.
3. R.C. Davidson, K.T. Tsang and H.S. Uhm, Phys. Fluids 31, 1727 (1988).
4. R.C. Davidson, Phys. Fluids 28, 1937 (1985).
5. R.C. Davidson, Phys. Fluids 27, 1804 (1984).
6. R.J. Briggs, J.D. Daugherty and R.H. Levy, Phys. Fluids 13, 421 (1970).
7. J.D. Daugherty, J.E. Eninger and G.S. Janes, Phys. Fluids 12, 2677 (1969).
8. R.H. Levy, Phys. Fluids 11, 920 (1968).
9. O. Buneman, R.H. Levy and L.M. Linson, J. Appl. Phys. 37, 3203 (1966).
10. R.H. Levy, Phys. Fluids 8, 1288 (1965).
11. O. Buneman, J. Electron. Control 3, 507 (1957).
12. C.C. MacFarlane and H.G. Hay, Proc. Phys. Soc. (London) 63B, 409 (1950).
13. S.A. Prasad and J.H. Malmberg, Phys. Fluids 29, 2196 (1986).
14. R.L. Kyhl and H.F. Webster, IRE Trans. Electron Devices ED-3, 172 (1956).
15. J.R. Pierce, IRE Trans. Electron Devices ED-3, 183 (1956).
16. C.A. Kapetanakos, D.A. Hammer, C. Striffler and R.C. Davidson, Phys. Rev. Letters 30, 1303 (1973).
17. G. Rosenthal, G. Dimonte and A.Y. Wong, Phys. Fluids 30, 3257 (1987).
18. G. Rosenthal and A.Y. Wong, "Localized Density Clumps and Potentials Generated in a Magnetized Nonneutral Plasma," UCLA Report No. PPG1282 (1989).
19. K.S. Fine, C.F. Driscoll and J.H. Malmberg, Phys. Rev. Lett. 63, 2232 (1989).
20. J.H. Malmberg, C.F. Driscoll, B. Beck, D.L. Eggleston, J. Fajans, K. Fine, X.-P. Huang and A.W. Hyatt, in Nonneutral Plasma Physics, eds., C.W. Roberson and C.F. Driscoll, AIP Conference Proceedings 175, 28 (1988).

21. C.F. Driscoll, J.H. Malmberg, K.S. Fine, R.A. Smith and X.-P. Huang, in Plasma Physics and Controlled Nuclear Fusion Research, Nice (IAEA, Vienna, 1989), Vol. 3, p. 507.
22. R.C. Davidson, Chapter 8 of Ref. 1.
23. J. Benford, in High-Power Microwave Sources, eds., V. Granatstein and I. Alexeff (Artech House, Boston, Massachusetts, 1987) p. 351.
24. J. Benford, H.M. Sze, W. Woo, R.R. Smith and B. Harteneck, Phys. Rev. Lett. 62, 969 (1989).
25. G. Bekefi and T.J. Orzechowski, Phys. Rev. Lett. 37, 379 (1976).
26. A. Palevsky and G. Bekefi, Phys. Fluids 22, 986 (1979).
27. T.J. Orzechowski and G. Bekefi, Phys. Fluids 22, 978 (1979).
28. A.G. Nokonov, I.M. Roife, Yu.M. Savel'ev and V.I. Engel'ko, Sov. Tech. Phys. 32, 50 (1987).
29. I.Z. Gleizer, A.N. Didenko, A.S. Sulakshin, G.P. Fomenko and V.I. Tsvetkov, Sov. Tech. Phys. Lett. 6, 19 (1980).
30. H.S. Uhm, H.C. Chen and R.A. Stark, Proc. SPIE 1061, 170 (1989).
31. Y.Y. Lau, in High-Power Microwave Sources, eds., V. Granatstein and I. Alexeff (Artech House, Boston, Massachusetts, 1987) p. 309.
32. S.P. Yu, G.P. Kooyers and O. Buneman, J. Appl. Phys. 36, 2550 (1965).
33. A. Palevsky, G. Bekefi and A.T. Drobot, J. Appl. Phys. 52, 4938 (1981).
34. A. Palevsky, et al., in High-Power Beams, eds., H.J. Doucet and J.M. Buzzi (Ecole Polytechnique, Palaiseau, France, 1981) p. 861.
35. H.-W. Chan, C. Chen and R.C. Davidson, "Computer Simulation of Multiresonator Cylindrical Magnetrons," submitted for publication (1990).
36. B. Goplen and J. McDonald, private communication (1989). The MAGIC simulation code was developed by researchers at Mission Research Corporation. The simulation results presented in this paper use the code version dated 1988.